ACS Catalysis

Research Article

pubs.acs.org/acscatalysis

# Application of Operando XAS, XRD, and Raman Spectroscopy for Phase Speciation in Water Gas Shift Reaction Catalysts

A. Patlolla,[†] E. V. Carino,[‡] S. N. Ehrlich,[§] E. Stavitski,*[,§] and A. I. Frenkel*[,†]

[†]Department of Physics, Yeshiva University, New York, New York 10016, United States

[‡]Department of Chemical Engineering, University of Delaware, Newark, Delaware 19716, United States

[§]National Synchrotron Light Source, Brookhaven National Laboratory, Upton, New York 11973, United States

**ABSTRACT:** The structural and compositional changes of the partially reduced iron oxide $Fe_2O_3$ and 3% chromium oxide-modified iron oxide (3% $Cr_2O_3/Fe_2O_3$) catalysts before, during, and after the water gas shift (WGS) reaction are reported. The measurements were performed by collecting X-ray absorption fine structure, X-ray diffraction, and Raman spectroscopy data on the catalysts and the mass spectrometry data of reactants and products, all done in a single experiment. These materials demonstrated marked structural disorder and compositional heterogeneity that are peaked in their catalytically active states. The main findings revealed in the result of combining multiple techniques include the role of Cr in stabilizing the low-temperature $\gamma$-$Fe_2O_3$ phase, the nature of the disordered phase in the active state of the catalysts, and the possible deactivation mechanism.

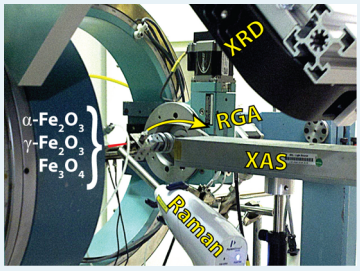


**KEYWORDS:** *catalysis, in situ, operando, combined techniques, XANES, EXAFS, XRD, Raman spectroscopy*

## 1. INTRODUCTION

In the past decade, many synchrotron techniques have been established with the sole purpose of improving time, energy, and space resolutions for the determination of structure, dynamics, and kinetics of catalytically active sites.[1,2] In parallel with the development of individual techniques, experimental approaches aimed at new and improved ways to investigate catalytic mechanisms in situ have evolved.[3,4] Today, the state of the art is conducting catalytic studies in situ or operando while combining complementary techniques in a single experiment.[5−8] As operando investigations expand their range from model catalysts to real system, new challenges arise. One of them is the presence of many competing factors that affect catalytic process: for example, heterogeneity of particle sizes and shapes,[9] temperature and pressure gradients,[3,10,11] support and adsorbate effects.[12,13] Another complication is the presence of multiple length scales that define a real catalytic system. In this work, we show how a combination of spectroscopic and scattering techniques can be added together to shed light on the processes that occur simultaneously at different length scales, from tens of picometers to micrometers. To demonstrate this approach, we chose an inherently complex catalytic system, a chromium oxide-modified iron oxide for high temperature water gas shift (WGS) reaction.

The WGS reaction is an important industrial process in which carbon monoxide reacts with steam to produce carbon dioxide and molecular hydrogen:

$$CO + H_2O \rightarrow CO_2 + H_2 \quad (1)$$

At industrial plants, the WGS reaction is usually carried out at two different temperature ranges, a high temperature (350−500 °C) and a low temperature (190−250 °C).[14] Iron oxide is one of the most commonly used commercial catalysts for the high temperature WGS reaction. Different phases observed during the reduction process of iron oxide at different temperature ranges include $Fe_2O_3$, $Fe_3O_4$, FeO, and Fe.[15] The catalytically active phase of iron oxide is $Fe_3O_4$, produced by the partial reduction of $Fe_2O_3$.[16] It is important to avoid overreduction of the $Fe_3O_4$ active materials to lower oxides, carbides of metallic iron species during reduction or reaction. The reason is that metallic iron species are active catalysts for highly exothermic methanation and Fischer−Tropsch processes that can damage the catalyst performance.[17] One possible cause of the overreduction is the combination of a low concentration of steam and higher than the optimal reaction temperatures.[17] In addition, pure magnetite catalysts rapidly loose activity due to the reduction in surface area caused by sintering. Hence, structural stabilizers, usually $Cr_2O_3$, are added to iron oxide.[16,18−24] Despite the industrial significance and numerous studies of the high-temperature WGS catalysts, little is known to date regarding the role of $Cr_2O_3$ additive in the stabilization of the catalyst structure, although it has been proposed[25,26] that the reduced catalyst forms an inverse spinel type structure with $Cr^{3+}$ ions in solid solution within the $Fe_3O_4$ lattice. This brief overview demonstrates the need to evaluate the state of the catalyst before, during, and after the optimum WGS conditions to understand the influence of synthetic conditions, temperature, and gas composition on the catalytic activity and selectivity.

**Special Issue:** Operando and In Situ Studies of Catalysis

**Received:** June 27, 2012
**Revised:** September 4, 2012
**Published:** September 17, 2012

 © 2012 American Chemical Society  dx.doi.org/10.1021/cs300414c | *ACS Catal.* 2012, 2, 2216−2223

Another challenge in the mechanistic understanding of the WGS reaction catalysis by iron oxides is the lack of consensus on the nature of reaction pathways. Extensive studies over the last two decades have suggested that the WGS reaction may involve two types of reaction mechanisms:[17,27,28] regenerative and associative. The regenerative, or redox, mechanism is based on the dissociation of water on the catalyst to produce hydrogen and subsequent oxidation of the catalyst surface. The surface is then reduced by carbon monoxide to produce carbon dioxide and thereby complete the catalytic cycle:[29,30]

$$H_2O + Red \rightarrow H_2 + Ox \quad (2)$$

$$CO + Ox \rightarrow CO_2 + Red \quad (3)$$

The associative mechanism is based upon the interaction of adsorbed carbon monoxide and water on the catalyst surface to form an intermediate, which breaks down to form reaction products:[27]

$$CO + H_2O \rightarrow (intermediate) \rightarrow CO_2 + H_2 \quad (4)$$

The importance of the redox mechanism in the high temperature catalysts has been confirmed by Boreskov[31] who showed that a $Fe^{2+}/Fe^{3+}$ coupling existed in $Cr_2O_3$–$Fe_3O_4$ catalysts, with $Fe^{2+}$ being oxidized to $Fe^{3+}$ by water and $Fe^{3+}$ being reduced by carbon monoxide. However, a number of theoretical[32−36] and experimental (redox[37,38] and associative[39,40]) studies have supported both mechanisms.

Such complex systems and reactions make a good case for the development and application of multi-technique experimental tools that investigate these problems simultaneously, in a single experiment, as opposed to one at a time. Several in situ studies combining different techniques have addressed the issues related to the structural changes of the different types of WGS catalysts,[41] catalytic active sites,[42] the role of promoters or stabilizers of the catalysts,[23,43] and reaction mechanisms.[17,20,26,27,29,31,44] Further progress in mechanistic investigations can be achieved by studying catalytic reactions under operando conditions by combining multi-technique studies with the monitoring of catalyst performance with online real time product analysis.[45−52]

X-ray absorption fine structure (XAFS), X-ray diffraction (XRD)[48,50] and Raman spectroscopy[47,51,52] provide complementary information on the structure and valence state of iron oxide during reaction. Raman spectrometers have been routinely used in conjunction with X-ray measurements at X-ray absorption spectroscopy (XAS) and XRD synchrotron beamlines at the European Synchrotron Radiation Facility (ESRF),[8] and specialized cells for combining these techniques together at the ESRF have been reported.[53] Other synchrotron facilities have yet to follow suit. The use of these methods is clearly advantageous for composite catalytic systems, such as metal oxide catalysts. For example, in $Fe_2O_3$ catalyst, the transformation of phases cannot be identified by EXAFS, but XRD and Raman spectra show clear distinctions between the phases.[54−56] Similarly, in 3% $Cr_2O_3/Fe_2O_3$, chromium oxide species could not be detected by XRD but give rise to broad vibrational bands in the Raman spectrum. In this work, we combined XAS/XRD/Raman measurements using the X18A beamline of the National Synchrotron Light Source (NSLS) at Brookhaven National Laboratory. The studies provide new information about the oxidation state, local atomic structure, crystal structure in the bulk and in the surface, before, during, and after WGS reaction. This work opens up new opportunities for similar operando studies of a large class of heterogeneous catalytic reactions.

## 2. EXPERIMENTAL SECTION

**Catalyst Preparation.** Two types of metal oxides—a pure iron oxide, and a chromium oxide/iron oxide system—were used for this work. The iron oxide used was a commercial $\alpha$-$Fe_2O_3$ (Alfa Aesar, 99%). The second system, containing chromium oxide, was prepared by incipient wetness impregnation of aqueous solutions of chromium(III) nitrate ($Cr(NO_3)_3{\cdot}9H_2O$, Alfa Aesar, 98.5%) and distilled water on an iron oxide support ($\alpha$-$Fe_2O_3$, Alfa Aesar, 99+%) using an incipient wetness point of ∼0.4 mL/g $Fe_2O_3$ under ambient conditions. This sample was prepared with a chromium loading of 3 wt % $CrO_3$. It was allowed to dry overnight under ambient conditions, followed by a second drying step exposed to flowing air at 100 °C for 4 h in a programmable furnace (Thermolyne, model 48000). Finally, the catalyst was subjected to calcination by ramping the temperature at 2 °C/min under flowing air (Airgas, Zero grade) to 350 °C for 2 h. The final synthesized catalyst is denoted as 3% $Cr_2O_3/Fe_2O_3$.

**X-ray Absorption Spectroscopy.** We used the same setup for combined XAFS and XRD measurements as the one described previously.[57] XAFS data were collected in transmission mode, using ionization chamber detectors for measuring incident and transmitted beam intensities. In addition, a third ionization chamber was used to detect the beam through a reference Fe foil for energy calibration and alignment purposes. In this work, we present results obtained for the Fe K-edge data only. Cr K-edge data measured in fluorescence will be described elsewhere.

**X-ray Diffraction.** XRD patterns were acquired with a Perkin-Elmer (PE) amorphous silicon detector having 2048 × 2048 pixels and a 200 × 200 $\mu m^2$ pixel size.[57] The wavelength of the beam was set to $\lambda$ = 0.124 nm. Before collecting the spectra, the detector was calibrated using a $LaB_6$ standard. For each spectrum, 10 exposures of 4 s duration were recorded for both the diffraction pattern and the dark current, and the dark current was subtracted. Plots of the $2\theta$ data were created from the recorded XRD patterns using the Datasqueeze software developed by Paul Heiney. The $2\theta$ plots were compared against the JCPDS reference library using the JADE software (MDI Products).

**Raman Spectroscopy.** Raman spectra were obtained using a Perkin-Elmer Raman station 400 series with 785 nm laser excitation. The spectrometer was calibrated using a silicon wafer to a frequency accuracy of ±1 $cm^{-1}$. We collected spectra only at room temperature, although future upgrades are envisioned that will enable corrections for spectral thermal broadening from high temperatures and visible light irradiation from the in situ cell heating element.

**Catalytic activity.** Operando experiments were performed in a Clausen cell,[58] which allows for the flow of reactant gases over the sample during the acquisition of XAFS, XRD, and Raman data. The sample powder was loosely packed into a 1.0 mm o.d./0.9 mm i.d. quartz capillary. The capillary was connected to 1/16 in. Swagelok style fittings with Vespel ferrules. An Omega thermocouple was inserted into the capillary and placed adjacent to and contacting the catalyst bed. The sample was aligned such that the sample closest to the thermocouple was simultaneously in the beam path for X-ray measurements and at the focus spot from the Raman optical probe. The X-ray beam size on the sample was 1 mm


dx.doi.org/10.1021/cs300414c | ACS Catal. 2012, 2, 2216−2223

(horizontally) × 1 mm (vertically); hence, the data were obtained after averaging over any gradients (temperature or pressure) within the sample. The reagent gases were passed into the quartz tube through an inlet, and the products were analyzed by using a mass spectrometer connected through an outlet. The catalyst sample was heated by using a resistive heater placed under the catalyst bed. $Fe_2O_3$ and 3% $Cr_2O_3$/$Fe_2O_3$ catalysts were initially activated in the 5−10% $O_2$ mixed with helium at a flow rate of 10 mL/min while ramping the temperature from room temperature (RT) to 400 °C. The activation was followed by the WGS reaction at 400 °C by passing 1.5% CO mixed with helium through a water bubbler before entering the reactor (3% $H_2O$). The relative ratio of steam to CO in the feed gas mixture was around 2:1. A typical process took a few hours, and during the entire process, the WGS reaction was monitored by using a mass spectrometer. After the reaction reached steady state, the catalyst was cooled to room temperature under the flow of the same gas mixture.

The composition of the reaction mixture at the outlet of the reactor was measured with a 0−100 amu quadruple mass spectrometer (QMS, Stanford Research Systems). A portion of the exit gas flow passed through a leak valve and into the QMS vacuum chamber. QMS signals at mass-to-charge ratios of 2 ($H_2$), 4 (He), 18 ($H_2O$), 28 (CO), and 44 ($CO_2$) were monitored during the experiments, and these were recorded at the same time by a computer.

Measurements by XRD, Raman, and XAFS were done consecutively, with about 1−5 min time delay between measurements. The time was needed to move the monochromator to the fixed energy for the XRD measurements after the end of the XAFS scan and to set up the Raman measurement after the end of the XRD measurement. Each XAFS scan duration was ∼15 min (up to 3−5 scans were collected for averaging to improve signal-to-noise ratio), and Raman and XRD measurements took ∼5 min each.

## 3. RESULTS AND DISCUSSION

Figure 1 displays a series of Fe K-edge XANES spectra collected after exposing $Fe_2O_3$ to $O_2$ at RT and 400 °C, during the WGS reaction at 400 °C and after the WGS reaction, in the WGM flow condition at RT. The Fe K-edge positions measured in $O_2$ flow at RT and 400 °C are similar, indicating the preservation of the charge state of Fe. The edge is shifted to the lower energy in WGM conditions at 400 °C compared with its oxidized state immediately prior to the WGS reaction. This shift is consistent with the partial reduction of Fe from $Fe_2O_3$ to $Fe_3O_4$. The Fe K-edge then shifts to the higher energy during the WGM flow condition. We explain this change by the oxidizing effect of steam at the temperatures lower than the WGS reaction temperature (below 200 °C) and the concomitant decrease in the reducing activity of CO. XANES alone, however, cannot identify nor can it resolve quantitatively the different fractions of iron oxide phases (e.g., $\alpha$-$Fe_2O_3$, $\gamma$-$Fe_2O_3$, or $Fe_3O_4$) that can all coexist at the same temperatures before, during, and after the reaction.

Figure 2 displays *k*-space (a) and *r*-space (b, c) for the series of Fe K-edge EXAFS spectra collected before and after the WGS reaction in both catalysts. The data demonstrates that both catalysts underwent significant changes in the local structural environment of Fe, although the changes were markedly different between the two systems. The intensity of the first peak located between 1 and 2.0 Å, which corresponds to the first Fe−O nearest neighbor (1NN) distance in both the

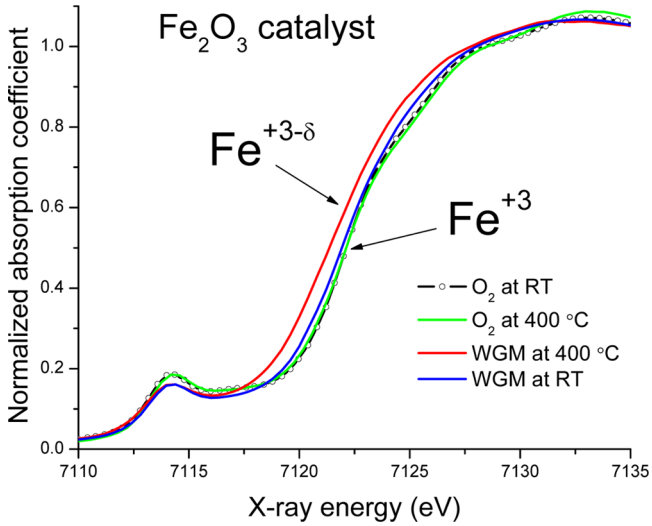


**Figure 1.** Normalized X-ray absorption coefficient in the XANES region of the Fe K-edge in $Fe_2O_3$ sample. Fe charge does not change until the WGM is introduced in the reactor at 400 °C. It then decreases isothermally, followed by partial reoxidation in WGM conditions when temperature is lowered to RT.

$Fe_2O_3$ and 3% $Cr_2O_3$/$Fe_2O_3$ catalysts, decreases after the WGS reaction. This reduction can be interpreted either by the decreased Fe−O coordination number or the increased bond length disorder or both.

The former factor cannot be too significant because the Fe−O environment in iron oxides ranges from purely octahedrally coordinated Fe atoms (e.g., $\alpha$-$Fe_2O_3$) to a mixture of two-thirds octahedrally coordinated and one-third tetrahedrally coordinated Fe atoms, as in $Fe_3O_4$ or a similar mixture in $\gamma$-$Fe_2O_3$.[59] That corresponds to a reduction of the coordination number of Fe−O bonds from 6 (in pure $\alpha$-$Fe_2O_3$) to $6(2/3) + 4(1/3) \approx 5.34$ (in pure $Fe_3O_4$). When the mixture of different iron oxide phases is present, as in our case (vide infra), the contrast in coordination numbers becomes so small that it cannot be reliably detected by EXAFS analysis.

The bond length disorder decreases the intensity of EXAFS oscillations due to the partial decoherence of photoelectron paths connecting the X-ray absorbing atoms and their nearest neighbors.[60] The decoherence is due to the mismatch in the bond lengths arising from the fact that the pair distribution function is broadened by the configurational, thermal disorder, or both. The disorder can be quantified by $\sigma$, the standard deviation in the bond length, $R$, commonly defined as $\sigma^2 = \langle (R - \bar{R})^2 \rangle$. In the case of small to moderate disorder, the radial distribution function can be approximated by a Gaussian.[61] The corresponding term in the EXAFS equation is $\exp(-2k^2\sigma^2)$, and it is that term that is responsible for the reduction in the EXAFS intensity caused by the bond length disorder. A common approach is to extract the disorder parameter by fitting the EXAFS equation to the data; however, this approach breaks down in the case of strong, non-Gaussian disorder where fitting methods relying on Gaussian approximation produce erroneous results.[61,62] Indeed, as demonstrated by Yevick and Frenkel,[62] if Gaussian approximation is assumed for theoretical fitting of EXAFS data obtained in an asymmetrically disordered system (for which even a third cumulant is not sufficient for the cumulant extension series to converge) the distances, the coordination numbers, and the disorder parameters will be all obtained incorrectly. The origin of such enhanced disorder in

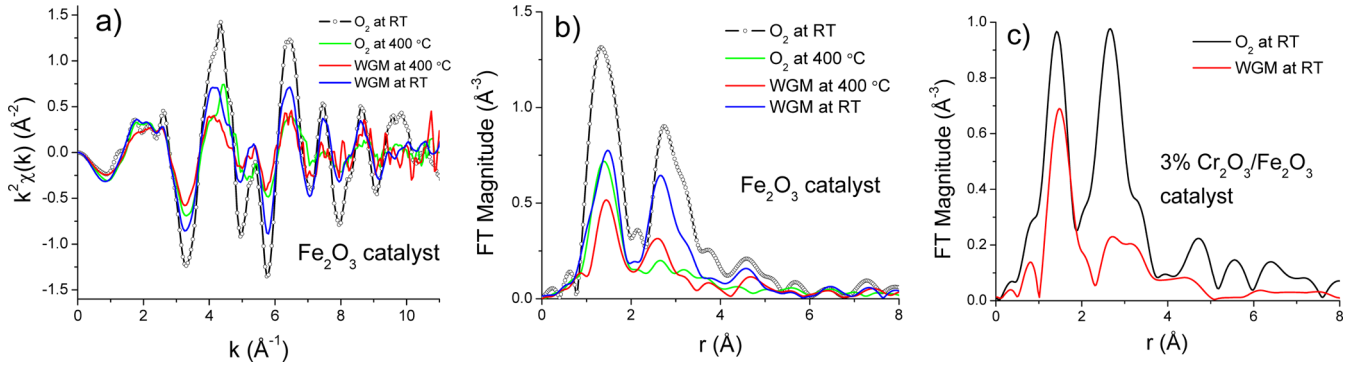


**Figure 2.** $k^2$-weighted Fe K-edge EXAFS spectra (a) and their Fourier transform magnitudes (b) for $Fe_2O_3$ collected during the flow of $O_2$ and WGM at RT and 400 °C. The *k*-range in Fourier transforms was from 2 to 10 $Å^{-1}$. (c) Fourier transform magnitudes of $k^2$-weighted Fe K-edge EXAFS spectra for 3% $Cr_2O_3/Fe_2O_3$ in the flow of $O_2$ and WGM at RT. The *k*-range in Fourier transforms was from 2 to 9 $Å^{-1}$.

the system described in this work is the coexistence of different iron oxide phases, each with its own distribution of Fe−O and Fe−Fe distances, as discussed in greater detail below.

The second peak in Figures 2b,c corresponds to the contributions of Fe−Fe bonds to Fe K-edge EXAFS. The reduction of the second peak in the Fourier transform magnitude of the EXAFS signal for the 3% $Cr_2O_3/Fe_2O_3$ sample compared with the $Fe_2O_3$ sample indicates a more heterogeneous mixture of different Fe oxide phases in the former sample, with different Fe−Fe distances. Discrimination between different forms of iron oxides is possible by quantitative EXAFS analysis that takes into account more distant neighbors,[63−65] but the important condition of phase homogeneity should be met for the results to be reliable.[66] In this work, XRD measurements show the coexistence of different Fe phases at different temperatures (vide infra), rendering fitting methods of EXAFS data analysis inconclusive.

Another result emerging from EXAFS data is the comparison of the data in $O_2$ at 400 °C and under the WGM conditions at the same temperature. The most notable effect is the decrease in the second peak intensity (Figure 2b) under $O_2$ compared with that under WGM conditions at the same temperature. Such behavior is consistent with the large disorder in Fe environment under $O_2$ prior to the onset of the WGS reaction. We will discuss the origin of this large disorder below.

Our interpretation of the EXAFS data is consistent with the in situ XRD results. Figure 3 displays XRD spectra acquired at different stages of the WGS reaction. The black line in Figure 3 a,b corresponds to the XRD spectra of the $Fe_2O_3$ and 3% $Cr_2O_3/Fe_2O_3$, respectively, at room temperature before the WGS reaction and indicates the presence of the pure $\gamma$-$Fe_2O_3$.[17] The Bragg peaks in the 3% $Cr_2O_3/Fe_2O_3$ sample are noticeably broader and weaker compared with the corresponding peaks of $Fe_2O_3$. This observation implies that the average particle size of the 3% $Cr_2O_3/Fe_2O_3$ catalyst is smaller than that in $Fe_2O_3$. The latter result is consistent with reports that the 3% $Cr_2O_3/Fe_2O_3$ samples prepared similarly to this work were found to have more surface area than the $Fe_2O_3$ particles.[19] No Bragg peaks of $Cr_2O_3$ could be detected, suggesting that chromium is embedded in the lattice of $Fe_2O_3$.[15] The red line in Figure 3b corresponds to the XRD pattern of 3% $Cr_2O_3/Fe_2O_3$ collected prior to the WGS reaction in the $O_2$ flow at 400 °C and indicates the appearance of the $\alpha$-$Fe_2O_3$ phase.[55] Such change is not noticeable by XRD in the $Fe_2O_3$ catalyst (red line, Figure 3a), as discussed in greater detail below. The incorporation of chromium has been shown in the literature to affect the high temperature reduction properties of the $Fe_2O_3$ bulk.[15] This effect may also be responsible for the presence of the two iron oxide polymorphs ($\alpha$- and $\gamma$-$Fe_2O_3$) observed at 400 °C with the Cr-doped sample (Figures 3b(ii), 5b(ii)).

Figure 4 shows an expanded view of the portion of the spectra between 48° and 51° in $2\theta$. The XRD spectra of both $Fe_2O_3$ and 3% $Cr_2O_3/Fe_2O_3$ during the WGS reaction at 400 °C (green line, Figure 4a,b) show a shift of the Bragg peak toward lower angles. This is consistent with the transformation from $\gamma$-$Fe_2O_3$ to $Fe_3O_4$, which has a larger lattice parameter. This observation also agrees well with the reduction of the iron oxide observed in XANES (Figure 1). Upon cooling, some oxidation of $Fe_3O_4$ to $Fe_2O_3$ is indicated by the shift of the Bragg peak toward higher angles (blue line, Figure 4a). It should be noted that the Bragg peak after the cooling (blue line) does not return to the same position as before heating (black line), meaning that the phase transition to $Fe_3O_4$ is not fully reversible under WGM flow. The main difference between the $Fe_2O_3$ and 3% $Cr_2O_3/Fe_2O_3$ catalyst systems is that the 3% $Cr_2O_3/Fe_2O_3$ undergoes transformations from $\gamma$-$Fe_2O_3$ to $\alpha$-$Fe_2O_3$ to $Fe_3O_4$, but in the case of the $Fe_2O_3$ catalyst, the transformation seems to progress directly from $\gamma$-$Fe_2O_3$ to $Fe_3O_4$ without the formation of $\alpha$-$Fe_2O_3$.

It turns out, however, that this picture is too simplified if only XRD data are used for phase speciation of the both catalysts. A combination of XRD and EXAFS results offers a more deep insight into the unique iron oxide phases and their transformations. The XRD data (Figure 3 b) show a fraction of $\alpha$-$Fe_2O_3$ present in the 3% $Cr_2O_3/Fe_2O_3$ sample and absent in the $Fe_2O_3$ sample (Figure 3a) in the beginning of the temperature ramp. Although the XRD peaks of the $\alpha$-$Fe_2O_3$ are absent during and after the WGS reaction, EXAFS data suggest that the low-dimensional component of $\alpha$-$Fe_2O_3$ or other octahedrally coordinated Fe compounds (e.g., $\gamma$-FeOOH) may be present throughout the temperature cycle in the $Cr_2O_3/Fe_2O_3$ system. Such a heterogeneous mixture of Fe compounds should cause larger disorder in Fe−Fe distances in the $Cr_2O_3/Fe_2O_3$ system and the concomitant reduction of the second peak intensity after the WGS reaction compared with the pure $Fe_2O_3$ (Figures 2b,c). The reason for that is the coexistent Fe phases have a larger spread in the Fe−Fe distances than a single phase as a result of the presence of face, corner, and edge-sharing octahedra.[59] A similar conclusion can be made regarding the $Fe_2O_3$ sample under $O_2$ flow at 400 °C: although the XRD peak of $\alpha$-$Fe_2O_3$ is barely visible in Figure 3a, EXAFS data (Figure 2b) indicate much larger disorder in the second


dx.doi.org/10.1021/cs300414c | ACS Catal. 2012, 2, 2216−2223

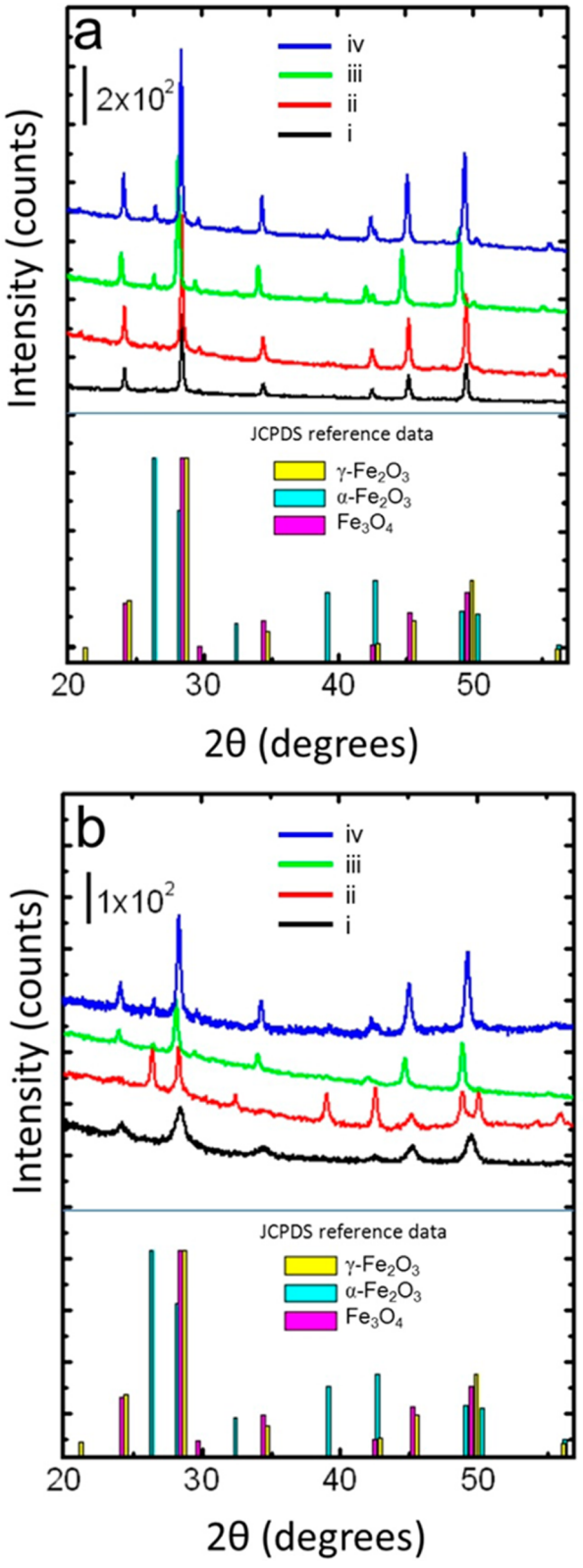


**Figure 3.** XRD spectra of (a) $Fe_2O_3$ and (b) 3% $Cr_2O_3/Fe_2O_3$ catalysts during the 4 reaction stages: (i) prior to the WGS reaction, in $O_2$ at RT; (ii) prior to the WGS reaction, in $O_2$ at 400 °C; (iii) during the WGS reaction at 400 °C; and (iv) after the WGS reaction, under WGM conditions at RT.

peak region compared with the data taken at the same temperature under WGM conditions, consistent with the presence of a strongly disordered or low dimensional phase such as $\alpha$-$Fe_2O_3$. It has been recently observed that XAFS is more sensitive to such disordered phases and detects their presence before XRD does, if the two techniques are used in the same experiment.[57] As shown below, Raman measurement also detects the presence of $\alpha$-$Fe_2O_3$ even at room temperature, confirming this model.

When the results of our measurements are interpreted self-consistently, a new and more complex picture of the phases and their transformation emerges (Table 1). Since analytical power of XRD method is limited when strongly dispersed or disordered species are present, we employed Raman spectroscopy to gain additional information about the phase mixture in the samples. Raman spectra of the $Fe_2O_3$ and 3% $Cr_2O_3/Fe_2O_3$ catalysts were collected at room temperature under the same conditions as the XAFS and XRD data discussed above. The Raman spectra of both catalysts before the WGS reaction are presented in Figure 5a. For $Fe_2O_3$, several peaks at 226, 244, 261, 292, 378, 496, and 635 $cm^{-1}$ are present before the catalyst is pretreated (hydrated state). Peaks at 226 and 292 $cm^{-1}$ can be assigned to $\alpha$-$Fe_2O_3$ phase, and the broad peak at 378 $cm^{-1}$ and the peaks at 244, 261, 496, and 635 $cm^{-1}$ most likely originate from a $\gamma$-$Fe_2O_3$ phase.[56] Alternatively, the peak at 261 $cm^{-1}$ could correspond to a $\gamma$-FeOOH phase. The Raman spectrum of 3% $Cr_2O_3/Fe_2O_3$, collected at room temperature before the WGS reaction, displays peaks at 378, 492, 632, and 830 $cm^{-1}$. The peaks at 378, 492, and 632 $cm^{-1}$ are most likely from the $\gamma$-$Fe_2O_3$ phase, as previously assigned above.[56] The peak appearing at 830 $cm^{-1}$ is from hydrated $CrO_4^{2-}$ oxoanions.[67]

Raman spectroscopy is more sensitive to oxide phases compared with XRD when the phase of interest exists in domains not exceeding ~4 nm in size. Since XRD did not detect the presence of $\alpha$-$Fe_2O_3$ phase (Figure 3a(i)) for the case of $Fe_2O_3$ catalyst, but Raman spectroscopy did (Figure 5a), that phase is most likely present as dispersed regions on the surface of the catalyst particles. This conclusion is also consistent with the EXAFS data behavior showing enhanced disorder in Fe−Fe distances at 400 °C under $O_2$ flow. The lack of Raman bands from $\alpha$-$Fe_2O_3$ for 3% $Cr_2O_3/Fe_2O_3$ suggests that the addition of chromium helps stabilize $\gamma$-$Fe_2O_3$ as a single polymorph at room temperature before the WGS reaction. Formation of bulk $\alpha$-$Fe_2O_3$ phase is evident in both samples at higher temperatures, as indicated by XRD and, more indirectly, by EXAFS (vide supra). The fact that the dispersed $\alpha$-$Fe_2O_3$ phase existed and that it existed only in the pretreated $Fe_2O_3$ sample are new and surprising results that could have not been obtained unless the in situ Raman spectroscopy experiment was performed.

Raman spectra of 3% $Cr_2O_3/Fe_2O_3$ before and after the WGS reaction are present in Figure 5b. The loss of the majority of the $CrO_4^{2-}$ 830 $cm^{-1}$ peak indicates that the doped $CrO_x$ species were almost completely and irreversibly reduced during the WGS reaction. This irreversible nature of the surface $CrO_x$ species suggests Cr dissolution into the bulk oxide support during the WGS reaction, as has been proposed in the literature.[21,26,29,30,44,68] This and other processes that are irreversible (e.g., the incomplete reoxidation of the $Fe_2O_3$ catalyst (Figure 1) and stabilization of the $\alpha$-$Fe_2O_3$ phase in the end of the cycle (Figure 3) are possible causes for the deactivation of the catalyst.

The benefit of measuring these transformations in operando conditions is highlighted in Table 1. It reveals the sequence of


dx.doi.org/10.1021/cs300414c | ACS Catal. 2012, 2, 2216−2223

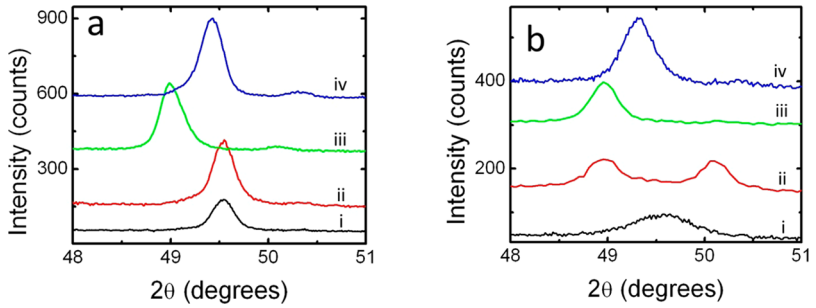


**Figure 4.** Expanded view of the XRD spectra of (a) $Fe_2O_3$ and (b) 3% $Cr_2O_3/Fe_2O_3$ catalysts during the four reaction stages: (i) prior to WGS reaction, in $O_2$ at RT; (ii) prior to WGS reaction, in $O_2$ at 400 °C; (iii) during the WGS reaction at 400 °C; and (iv) after the WGS reaction, in WGM conditions, at RT. The peak at ~50.2° corresponds to the $\alpha$-$Fe_2O_3$ phase.

**Table 1. Different Phases in $Fe_2O_3$ Catalyst Identified by Complementary Techniques before, during and after the WGS Reaction**

| | XAS | XRD | Raman |
|---|---|---|---|
| RT in $O_2$ | $Fe_2O_3$[a] | $\gamma$-$Fe_2O_3$ | $\alpha$-$Fe_2O_3$/ $\gamma$-$Fe_2O_3$ |
| 400 °C in $O_2$ | $Fe_2O_3$[a] (strong Fe−Fe bond length disorder, consistent with phase mixture) | $\gamma$-$Fe_2O_3$ | |
| 400 °C in WGM | $Fe_3O_4$[a] | $Fe_3O_4$ | |
| RT in WGM | $Fe_2O_3$[a] (incompletely reoxidized) | $\gamma$-$Fe_2O_3$/ $\alpha$-$Fe_2O_3$[b] | $\gamma$-$Fe_2O_3$ |

[a] $\gamma$ and $\alpha$ phases cannot be discriminated on the basis of XANES analysis. [b] Very weak reflection for $\alpha$-$Fe_2O_3$

transformations, the degree of crystalline order, and the relevant experimental probes that were used to detect them.

In conclusion, the experiments succeeded in monitoring the changes between different phases of the catalyst in the course of the reaction cycle and revealed relationships between different processes. First, we observed that the production of $CO_2$ and $H_2$ follows the activation of the oxide samples $Fe_2O_3$ and 3% $Cr_2O_3/Fe_2O_3$ via their partial reduction by CO at 400 °C. When the catalyst was cooled to RT in the same gas flow (CO and $H_2O$) conditions, it was partially reoxidized. This process might have been caused by the oxidation due to the steam present in the water gas mixture. Second, we report contrasting structural details accompanying the WGS reaction in both catalytic systems. One effect is the dramatic loss of crystalline order in the 3% $Cr_2O_3/Fe_2O_3$ oxide catalyst compared with the $Fe_2O_3$ system in the active state of the reaction. A possible explanation is due to the stabilization of enhanced surface area of the particle by chromium oxide and thereby the enhancement of the structural disorder, a mechanism previously discussed in the literature.[69] Another effect is the coexistence of multiple forms of low dimensional and strongly disordered phases with bulk forms of iron oxides, in which both the composition and temperature dependence are strongly sample-specific.

This study demonstrates the analytical power of combinations of complementary methods in studying mechanisms of catalytic activity, selectivity, and deactivation of real catalytic systems that possess compositional heterogeneity and a large range of spatial dimensions. The two examples of catalytic systems studied here (pure and chromium oxide-stabilized iron oxides) have utilized a particular combination (XAS/XRD/Raman/MS) of techniques, ones specifically chosen to expand

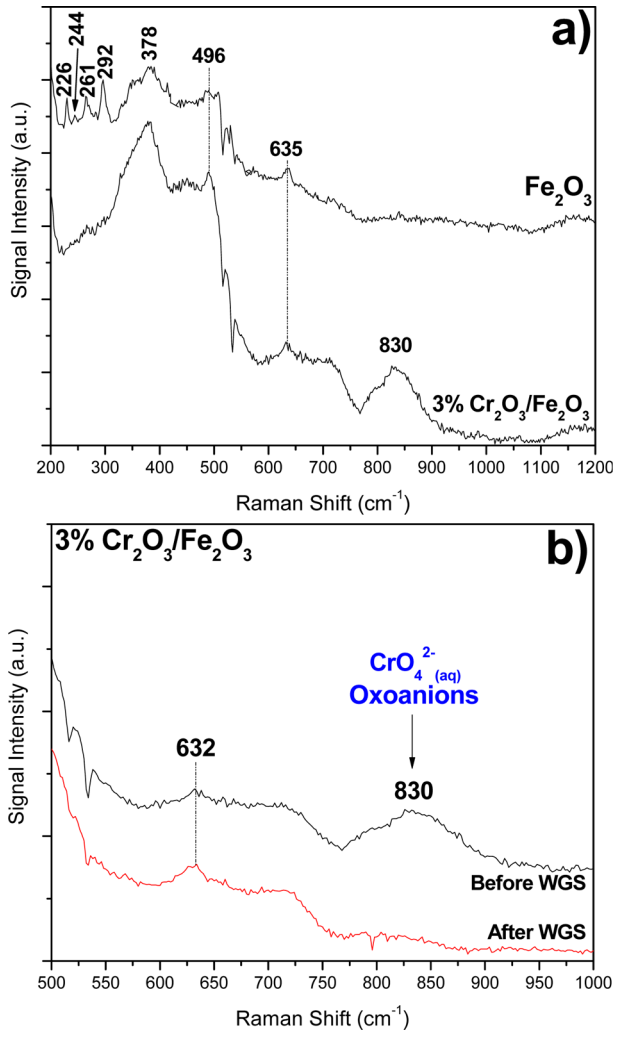


**Figure 5.** In situ Raman spectra of (a) both catalysts before WGS reaction and (b) chromium oxoanion region of 3% $Cr_2O_3/Fe_2O_3$ before and after the WGS reaction. Raman spectra were collected at room temperature.

the range of spatial dimensions where chemical transformations occur. We showed that only because of the complementary sensitivities of XANES and EXAFS to the local (on a scale of a few interatomic distances) and those of XRD to the average (on a scale of several unit cells) structural and electronic correlations, was the coexistence of ordered and disordered phases revealed in these systems. Raman spectroscopy was an important addition that allows investigation of the role of


dx.doi.org/10.1021/cs300414c | ACS Catal. 2012, 2, 2216−2223

catalytic components with low loading (promoters and stabilizers) such as the ones (chromium oxides) used in this work. Although the Raman data shown in this work were collected only at room temperature, we have recently performed a high temperature operando Raman experiment on a similar system that will be presented elsewhere.

## AUTHOR INFORMATION


### Corresponding Author

*E-mails: anatoly.frenkel@yu.edu, istavitski@bnl.gov.


### Notes

The authors declare no competing financial interest.

## ACKNOWLEDGMENTS

The authors are grateful to Prof. I. Wachs and C. Keturakis for sample preparation and for useful discussions and to Dr. Q. Wang for beamline support. A.I.F. and A.P. acknowledge the support of this work by the U.S. Department of Energy (DOE), Grant No. DE-FG02-03ER15476. E.C. is supported by the Synchrotron Catalysis Consortium (U.S. DOE Grant No. DE-FG02-05ER15688). Beamline X18A is supported in part by the U.S. DOE Grant No. DE-FG02-05ER15688. NSLS is supported by the U.S. DOE Grant No. DE-AC02-98CH10866.

## REFERENCES


(1) Thomas, J. M.; Sankar, G. *Acc. Chem. Res.* **2001**, *34*, 571−581.
(2) Bare, S. R.; Ressler, T. *Adv. Catal.* **2009**; *52*, 339−465.
(3) Grunwaldt, J.-D.; Kimmerle, B.; Baiker, A.; Boye, P.; Schroer, C. G.; Glatzel, P.; Borca, C. N.; Beckmann, F. *Catal. Today* **2009**, *145*, 267−278.
(4) Beale, A. M.; van der Eerden, A. M. J.; Jacques, S. D. M.; Leynaud, O.; O'Brien, M. G.; Meneau, F.; Nikitenko, S.; Bras, W.; Weckhuysen, B. M. *J. Am. Chem. Soc.* **2006**, *128*, 12386−12387.
(5) Tinnemans, S. J.; Mesu, J. G.; Kervinen, K.; Visser, T.; Nijhuis, T. A.; Beale, A. M.; Keller, D. E.; van der Eerden, A. M. J.; Weckhuysen, B. M. *Cat. Today* **2006**, *113*, 3−15.
(6) O'Brien, M. G.; Beale, A. M.; Jacques, S. D. M.; Weckhuysen, B. M. *Top. Catal.* **2009**, *52*, 1400−1409.
(7) Bentrup, U. *Chem. Soc. Rev.* **2010**, *39*, 4718−4730.
(8) Newton, M. A.; van Beek, W. *Chem. Soc. Rev.* **2010**, *39*, 4845−4863.
(9) Espinosa-Alonso, L.; O'Brien, M. G.; Jacques, S. B. M.; Beale, A. M.; de Jong, K. P.; Barnes, P.; Weckhuysen, B. M. *J. Am. Chem. Soc.* **2009**, *131*, 16932−16938.
(10) Grunwaldt, J.-D.; Hannemann, S.; Schroer, C. G.; Baiker, A. *J. Phys. Chem. B* **2006**, *110*, 8674−8680.
(11) Urakawa, A.; Baiker, A. *Top. Catal.* **2009**, *52*, 1312−1322.
(12) Frenkel, A. I.; Yang, J. C.; Johnson, D. D.; Nuzzo, R. G., Complexity of Nanoscale Atomic Clusters. In *Encyclopedia of Complexity and Systems Science*; Meyers, R. A., Ed.; Springer: New York: 2009; pp 5889−5912.
(13) Small, M. W.; Sanchez, S. I.; Marinkovic, N. S.; Frenkel, A. I.; Nuzzo, R. G. *ACS Nano* **2012**, *6*, 5583−5595.
(14) Tonkovich, A. Y.; Zilka, J. L.; LaMont, M. J.; Wang, Y.; Wegeng, R. S. *Chem. Eng. Sci.* **1999**, *54*, 2947−2951.
(15) Reddy, G. K.; Gunasekara, K.; Boolchand, P.; Smirniotis, P. G. *J. Phys. Chem. C* **2010**, *115*, 920−930.
(16) Gonzalez, J. C.; Gonzalez, M. G.; Laborde, M. A.; Moreno, N. *Appl. Catal.* **1986**, *20*, 3−13.
(17) Rhodes, C.; Hutchings, G. J.; Ward, A. M. *Catal. Today* **1995**, *23*, 43−58.
(18) Doppler, G.; Trautwein, A. X.; Ziethen, H. M.; Ambach, E.; Lehnert, R.; Sprague, M. J.; Gonser, U. *Appl. Catal.* **1988**, *40*, 119−130.
(19) Domka, F.; Basinka, A.; Fieldcrow, R. *Surf. Technol.* **1983**, *18*, 275.
(20) Edwards, M. A.; Whittle, D. M.; Rhodes, C.; Ward, A. M.; Rohan, D.; Shannon, M. D.; Hutchings, G. J.; Kiely, C. J. *Phys. Chem. Chem. Phys.* **2002**, *4*, 3902−3908.
(21) Chinchen, G. C.; Logan, R. H.; Spencer, M. S. *Appl. Catal.* **1984**, *12*, 69−88.
(22) Rhodes, C.; Hutchings, G. J. *Phys. Chem. Chem. Phys.* **2003**, *5*, 2719−2723.
(23) Kappen, P.; Grunwaldt, J. D.; Hammershøi, B. S.; Tröger, L.; Clausen, B. S. *J. Catal.* **2001**, *198*, 56−65.
(24) Chen, L. S.; Lü, G. L. *J. Mater. Sci.* **1999**, *34*, 4193−4197.
(25) Keiski, R. L.; Salmi, T. *Appl. Catal. A* **1992**, *87*, 185−203.
(26) Topsøe, H.; Boudart, M. *J. Catal.* **1973**, *31*, 346−359.
(27) Newsome, D. S. *Catal. Eng. Sci. Rev.* **1980**, *21*, 275−318.
(28) Amstrong, E. F.; Hilditcth, T. P. *Proc. R. Soc. London, Ser. A* **1920**, *97*, 265−273.
(29) Tinkle, M.; Dumesic, J. A. *J. Catal.* **1987**, *103*, 65−78.
(30) Keiski, R. L.; Niemisto, P.; Ainassaari, J.; Pohjola, V. J.; Salmi, T. *Appl. Catal. A* **1996**, *137*, 349−370.
(31) Boreskov, G. K. *Kinet. Katal.* **1970**, *11*, 374−382.
(32) Liu, P.; Rodriguez, J. A. *J. Chem. Phys.* **2007**, *126*, 164705.
(33) Rodriguez, J. A.; Liu, P.; Hrbek, J.; Evans, J.; Pérez, M. *Angew. Chem., Int. Ed.* **2007**, *46*, 1329−1332.
(34) Wang, G.; Jiang, L.; Cai, Z.; Pan, Y.; Zhao, X.; Huang, W.; Xie, K.; Li, Y.; Sun, Y.; Zhong, B. *J. Phys. Chem. B* **2003**, *107*, 557−562.
(35) Grabow, L. C.; Gokhale, A. A.; Evans, S. T.; Dumesic, J. A.; Mavrikakis, M. *J. Phys. Chem. C* **2008**, *112*, 4608−4617.
(36) Schumacher, N.; Boisen, A.; Dahl, S.; Gokhale, A. A.; Kandoi, S.; Grabow, L. C.; Dumesic, J. A.; Mavrikakis, M.; Chorkendorff, I. *J. Catal.* **2005**, *229*, 265−275.
(37) Koryabkina, N. A.; Phatak, A. A.; Ruettinger, W. F.; Farrauto, R. J.; Ribeiro, F. H. *J. Catal.* **2003**, *217*, 233−239.
(38) Ovesen, C. V.; Stoltze, P.; Nørskov, J. K.; Campbell, C. T. *J. Catal.* **1992**, *134*, 445−468.
(39) Campbell, C. T.; Daube, K. A. *J. Catal.* **1987**, *104*, 109−119.
(40) Grenoble, D. C.; Estadt, M. M.; Ollis, D. F. *J. Catal.* **1981**, *67*, 90−102.
(41) Wang, X.; Rodriguez, J. A.; Hanson, J. C.; Perez, M.; Evans, J. *J. Chem. Phys.* **2005**, *123*, 221101.
(42) Wang, X.; Rodriguez, J. A.; Hanson, J. C.; Gamarra, D.; Martínez-Arias, A.; Fernández-García, M. *J. Phys. Chem. B* **2006**, *110*, 428−434.
(43) Estrella, M.; Barrio, L.; Zhou, G.; Wang, X.; Wang, Q.; Wen, W.; Hanson, J. C.; Frenkel, A. I.; Rodriguez, J. A. *J. Phys. Chem. C* **2009**, *113*, 14411−14417.
(44) Robbins, M.; Wertheim, G. K.; Sherwood, R. C.; Buchanan, D. N. E. *J. Phys. Chem. Solids* **1971**, *32*, 717−729.
(45) Bruckner, A. *Chem. Commun.* **2001**, 2122−2123.
(46) Weckhuysen, B. M.; Baetens, D.; Schoonheydt, R. A. *Angew. Chem., Int. Ed.* **2000**, *39*, 3419−3422.
(47) Weckhuysen, B. M. *Phys. Chem. Chem. Phys.* **2003**, *5*, 4351−4360.
(48) Sankar, G.; Thomas, J.; Catlow, C. *Top. Catal.* **2000**, *10*, 255−264.
(49) Sankar, G.; Thomas, J. M. *Top. Catal.* **1999**, *8*, 1−21.
(50) Grunwaldt, J. D.; Clausen, B. S. *Top. Catal.* **2002**, *18*, 37−43.
(51) Banares, M. A.; Guerrero-Perez, M. O.; Fierro, J. L. G.; Cortez, G. G. *J. Mater. Chem.* **2002**, *12*, 3337−3342.
(52) Guerrero-Pérez, M. O.; Bañares, M. A. *Catal. Today* **2004**, *96*, 265−272.
(53) Tromp, M.; Russu, S.; Dent, A. J.; Mosselmans, J. F. W.; Harvey, I.; Hayama, S.; Russell, A. E.; Guerin, S.; Hayden, B. E.; Suchsland, J.-P.; Meacham, K.; Surridge, M.; Frey, J. G.; Tsapatsaris, N.; Beesley, A. M.; Schroeder, S. L. M.; Newton, M. A.; Fiddy, S.; Safonova, O. V.; Glatzel, P.; Binsted, N.; Evans, J. In *AIP Conference Proceedings*, Proceedings of X-Ray Absorption Fine Structure - XAFS 13; Stanford, California, July 9−14, 2006; Hedman, B., Pianetta, P., Eds.; Melville, New York, 2007; Vol. *882*, pp 858−860.
(54) Lee, Y.; Lee, J.; Bae, C. J.; Park, J. G.; Noh, H. J.; Park, J. H.; Hyeon, T. *Adv. Funct. Mater.* **2005**, *15*, 503−509.

(55) Hyeon, T.; Lee, S. S.; Park, J.; Chung, Y.; Na, H. B. *J. Am. Chem. Soc.* **2001**, *123*, 12798−12801.
(56) de Faria, D. L. A.; Venâncio Silva, S.; de Oliveira, M. T. *J. Raman Spectrosc.* **1997**, *28*, 873−878.
(57) Frenkel, A. I.; Wang, Q.; Marinkovic, N.; Chen, J. G.; Barrio, L.; Si, R.; Cámara, A. L.; Estrella, A. M.; Rodriguez, J. A.; Hanson, J. C. *J. Phys. Chem. C* **2011**, *115*, 17884−17890.
(58) Clausen, B. S.; Steffensen, G.; Fabius, B.; Villadsen, J.; Feidenhans, R.; Topsøe, H. *J. Catal.* **1991**, *132*, 524−535.
(59) Cornell, R. M.; Schwertmann, U., *The Iron Oxides: Structure, Properties, Reactions, Occurrences and Uses*; VCH: Weinheim, New York, 1996.
(60) Stern, E. A.; Heald, S. M. Basic Principles and Applications of EXAFS. In *Handbook of Synchrotron Radiation*; Koch, E. E., Ed.; North-Holland: New York, 1983; pp 995−1014.
(61) Crozier, E. D.; Rehr, J. J.; Ingalls, R. Amorphous and Liquid Systems. In *X-ray absorption spectroscopy*, Koningsberger, D. C., Prins, R., Eds.; John Wiley and Sons: New York, 1988; pp 373−442.
(62) Yevick, A.; Frenkel, A. I. *Phys. Rev. B* **2010**, *81*, 115451.
(63) Jiao, F.; Harrison, A.; Jumas, J.-C.; Chadwick, A. V.; Kockelmann, W.; Bruce, P. G. *J. Am. Chem. Soc.* **2006**, *128*, 5468−5474.
(64) Liu, T.; Guo, L.; Tao, Y.; Hu, T. D.; Xie, Y. N.; Zhang, J. *Nanostruct. Mater.* **1999**, *11*, 1329−1334.
(65) Subías, G.; García, J.; Blasco, J. *Phys. Rev. B* **2005**, *71*, 155103.
(66) Wang, Q.; Hanson, J. C.; Frenkel, A. I. *J. Chem. Phys.* **2008**, *129*, 234502.
(67) Weckhuysen, B. M.; Wachs, I. E. *Faraday Trans.* **1996**, *92*, 1969−1973.
(68) Rangel, M. d. C.; Sassaki, R. M.; Galembeck, F. *Catal. Lett.* **1995**, *33*, 237−254.
(69) Natesakhawat, S.; Wang, X.; Zhang, L.; Ozkan, U. S. *J. Mol. Catal. A: Chem.* **2006**, *260*, 82−94.